

95-193

Environment Canada

Water Science and
Technology Directorate

Direction générale des sciences
et de la technologie, eau

Environnement Canada

Bubbles Entrained by Mechanically Generated
Breaking Waves

By:

M. Loewen, M. O'Dor, M. Skafel

TD
226
N87
No. 95-
193

Bubbles Entrained by Mechanically Generated Breaking Waves

M.R. Loewen and M.A. O'Dor
Environmental Fluid Dynamics Laboratory
Department of Mechanical Engineering
University of Toronto
Canada

M.G. Skafel
National Water Research Institute
Canada Centre for Inland Waters
Burlington, Ontario
Canada

Abstract

A photographic technique was used to make measurements of the size distributions of large bubbles entrained by mechanically generated breaking waves in fresh- and saltwater. Digital video images of the region immediately beneath and behind the breaking wave crest were analyzed. This imaging technique was accurate for bubble radii, $r \geq 0.8$ mm. The magnitude and shape of the bubble size distributions were approximately the same in fresh- and saltwater. The bubble size distributions are well represented by an exponential equation of the form $N \sim e^{-1.5r}$ or by a power law equation of the form $N \sim r^{-3.7}$. There were no significant differences observed between the depth distribution of the bubbles in salt- and freshwater. In both cases the data can be represented by, $N = N_0 e^{-z/h}$ where z is the distance below the free surface, h is the entrainment depth and N_0 is the total bubble concentration at the free surface. N_0 and h were found to be 4×10^5 per m^3 and 1.0 cm respectively. The fact that significant numbers of large bubbles are entrained by relatively small breaking waves (wavelength ~ 1.5 m) suggests that gas transfer due to large entrained bubbles may be important even at low wind speeds.

1. Introduction

Bubbles entrained by breaking waves have a significant impact on a many physical, chemical and biological processes occurring at the air-water interface. Field experiments have shown that enhanced air-sea gas exchange may be caused by the increased air entrainment associated with breaking waves [Farmer, McNeil and Johnson, 1993; Wallace and Wirick, 1992]. Entrained bubbles rise back to the water surface and burst producing marine aerosols in the atmospheric surface layer [Blanchard and Woodcock, 1980]. Rising bubbles scavenge organic material and bacteria from the water column and transport it to the surface [Blanchard and Syzdek, 1972]. Breaking waves dissipate up to 40% of their energy and it has been found that up to 50% of the energy lost is expended in entraining air bubbles [Rapp and Melville, 1990; Lamarre and Melville, 1991]. The individual bubbles as well as the clouds of bubbles are significant sources and scatterers of sound in the upper ocean [Kerman, 1988].

Bubble plumes entrained by breaking waves evolve very rapidly in time. In energetic plunging breakers the average void fraction (the volume fraction of air in the total volume) decreases from 30-40% to approximately 1% in the first wave period

following breaking [Lamarre and Melville, 1991]. This rapid degassing of the plume is caused by the larger bubbles rising quickly back to the free surface. After the high void fraction plume has degassed a diffuse cloud of microbubbles is left behind. These microbubbles can persist in the water for long periods of time because they have small rise velocities and are easily advected by currents. At higher wind speeds these diffuse clouds are so numerous that a bubbly layer is formed beneath the free surface [Farmer and Vagle, 1989]. Within this bubbly layer a background bubble size distribution exists which varies slowly in time and space.

There have been numerous experiments conducted to measure background bubble size distributions in the upper ocean [[Blanchard and Woodcock, 1957; Johnson and Cooke, 1979; Kolovayev, 1976; Su, Ling and Cartmill, 1988]. However, measurements of the bubble size distributions inside the transient bubble plumes are scarce. This is due to several factors; (i) deploying instruments at sea when breaking waves are present is difficult, (ii) positioning a sensor just below the free surface without introducing a significant obstruction to the flow may not be possible, (iii) even at high wind speeds an individual sensor will only intersect a few breaking waves per hour, and (iv) many measurement techniques require averaging over time intervals significantly longer than typical wave periods.

Medwin and Breitz [1989] were able to overcome some of these difficulties by deploying an acoustic resonator from a small triangular buoy. They were able to measure the size of bubbles from 30 μm to 300 μm in radius at a depth of 25 cm. They found that bubble densities for $r < 50 \mu\text{m}$ varied as r^{-4} and that for $r > 60 \mu\text{m}$ they varied as $r^{-2.6}$. Their measurements were taken at windspeeds from 12 to 15 m/s in the open ocean. Cartmill and Su [1993] used an acoustic resonator to measure the bubble size distributions under salt- and freshwater breaking waves in a laboratory wave tank. They present only average bubble distributions at depths of 0.3 m and 0.73 m. Their averaged measurements showed that N the number of bubbles per m^3 per μm radius varied as $r^{-3.0}$ for bubble radii from 0.2 mm to 1.2 mm.

Measurements of the size distributions of large bubbles have been made under simulated breaking waves such as waterfalls and tipping buckets by Monahan and Zietlow, [1969], Cipriano and Blanchard [1981] and Haines and Johnson [1995]. Observations of the large bubbles entrained by breaking wind waves in laboratory tanks have been reported by Baldy and Bourguel [1987], Baldy [1988] and Hwang et al [1990]. Baldy and Bourguel [1987] and Baldy [1988] used a laser-based single particle technique to measure bubble sizes in freshwater between the troughs and crests of wind waves in a wind-wave channel. Their main conclusions were: (i) A bubble generation layer exists immediately below the free surface and below this is the dispersion layer dominated by turbulence and buoyancy effects; (ii) In the generation layer the slope of the bubble size spectrum is constant and approximately equal to -2; (iii) In the dispersion layer the slope of the size spectrum increases with depth approaching a value of -4; (iv) In the generation layer the bubble concentration increases exponentially with elevation as the free surface is approached. Hwang et al [1990] used an optical sensor based on the light blocking principle to measure bubble sizes in freshwater in a wind-wave channel. Their measurements were restricted to the region below the troughs of the waves. They observed an exponential decrease in the total bubble concentration with depth and found that the entrainment depth h (the e-folding depth) increased with wave amplitude. The slope of the bubble size spectrum increased with increasing depth from approximately -2 to -4.

Keeling [1993] recently used a model of bubble-induced gas exchange to investigate the role of large bubbles in air-sea gas exchange. He concluded that bubbles greater than 0.5 mm in radius contribute significantly to bubble-induced air-sea gas exchange. In addition, his results suggest that the majority of the enhanced air-sea gas transfer observed at windspeeds greater than 13 m/s is due to bubble entrainment by breaking waves. He noted that there is large degree of uncertainty in predictions of the

bubble-induced air-sea gas exchange because of a lack of data on the production rates and size distributions of large bubbles (radius greater than 0.5 mm).

We have addressed this issue by conducting a series of laboratory experiments to measure the bubble size distributions of large bubbles (0.8 - 5.0 mm radius) produced by mechanically generated breaking wave packets in fresh- and saltwater. Preliminary results from these experiments have been presented in *Loewen, O'Dor and Skafel* [1995].

2. Experimental Procedure

The experiments were conducted in a wave channel located at the Canada Centre for Inland Waters, Burlington, Ontario. The glass walled channel was 10 m long and the test section of the channel where the measurements were made was 30 cm wide and was filled with water to a depth of 40 cm. A computer controlled hinged hydraulic wave paddle was located in an enlarged steel-walled section at the end of the channel. The larger section was smoothly contracted to the dimensions of the test section as shown in figure 1. The wave paddle was programmed to focus a dispersive wave packet at a point $x_b = 5.8$ m from the wave paddle. This technique has been extensively used to investigate the behavior of spilling and plunging deep-water breaking waves [*Chan and Melville*, 1988; *Rapp and Melville*, 1990; *Loewen and Melville*, 1991]. Measurements were made of the water and air temperatures, surface displacement (fractional energy dissipation) and underwater sound. A detailed schematic of the experimental equipment is plotted in figure 1. Video recordings of the breaking waves were used to determine the size and location of entrained bubbles. Experiments were conducted in both fresh- and saltwater. The saltwater was 3.4% concentration by weight produced by adding NaCl to fresh tap water.

2.1 Breaking Wave Generation

A wave packet was synthesized from 32 sinusoidal components of constant slope ak , where a is the component amplitude and k is the component wavenumber. The wave components were equally spaced over a frequency bandwidth of $\Delta f = 0.7$ Hz and centred at a frequency of $f_c = 1.12$ Hz. Linear wave theory predicts a range in wavelengths from 0.64 m to 2.16 m for frequencies of $1.12 \text{ Hz} \pm 0.35 \text{ Hz}$. Breaking waves were generated using a personal computer and DAC (digital to analog converter) to convert a synthesized digital signal to an analog signal which was transmitted to the wave paddle hydraulic controller, see figure 1. This technique produces very repeatable breaking events and allows measurements to be averaged over repeated runs with the same breaking wave.

It has been shown by *Rapp and Melville* [1990] that deep water breaking is a function of three dimensionless parameters; a bandwidth parameter $\Delta f/f_c$, a phase parameter $x_b k_c$ and a slope parameter S . Their experiments showed that the dependence on $\Delta f/f_c$ and $x_b k_c$ was weak and that the dissipation due to wave breaking depended most strongly on the slope parameter S of the packet which is proportional to G the gain of the voltage signal transmitted to the wave paddle. In the present experiments, $\Delta f/f_c$ and $x_b k_c$ were held constant at 0.63 and 30.2 respectively, and G was varied in order to vary the intensity of the breaking events. Larger amplitude (steeper) wave packets break more intensely, that is, they dissipate more energy, entrain more air and generate more underwater sound [*Lamarre and Melville*, 1994; *Loewen and Melville*, 1994]. Below a low enough amplitude referred to as the threshold amplitude the packet does not break.

2.2 Surface Displacement Measurements

The surface displacement in freshwater was measured with a set of resistance wave gauges and digitally sampled at a rate of 40 Hz. The wave gauges and signal conditioning electronics supplied by HR Wallingford Limited (Wallingford, U.K.). The sensing elements were two 610 mm long, 6 mm diameter stainless steel rods mounted 50 mm apart on a supporting frame. An AC excitation (4.6 kHz) is transmitted through the

rods and then amplified, demodulated and filtered to produce a DC signal proportional to the submerged depth of the rods. Aliasing of the signals was prevented by filtering the analog signals with a low pass filter with -3 dB cut-off frequency of 20 Hz prior to digitizing.

The wave gauges were calibrated by sampling the still water level for 20 seconds at 6 vertical positions from -8 cm to +10 cm. A linear equation was fitted to the average voltage at each amplitude to give a calibration equation relating the voltage to the surface displacement. The correlation coefficient was always ≥ 0.99999 indicating that the gauges response was linear. The gauges were calibrated approximately every three hours in order to minimize the errors due to variations in the calibration coefficients. It was observed that air bubbles built up slowly on the surface of the stainless steel rods changing the response of the gauges. This problem was eliminated by wiping the bubbles off the rods with a cloth every third run. Runs were separated by three minutes to allow surface oscillations in the channel to decay to negligible amplitudes.

The repeatability of the wave packets was monitored by measuring the position of the wave paddle. The wave maker system included a position transducer which produced an analog signal proportional to the linear position of the paddle. This signal was sampled at 40 Hz along with the wave gauge signals and the variance was checked to ensure that repeated runs of the same wave packet slope produced equal variances.

Measurements of the surface displacement in saltwater were made using video recordings. A video camera was placed so that it viewed the free surface of the water through the sidewall of the channel. The camera lens was adjusted so that the field of view included 10 cm above and below the water surface. The digital video images normally have a resolution of 480 pixels in the vertical direction and 640 pixels in the horizontal direction. In order to maximize the resolution the camera was rotated 90 degrees so that the resolution in the vertical direction was 640 pixels. The water surface was easily distinguished in the video images because the meniscus appeared as a dark line. The surface displacement data was obtained from the video recordings by digitizing a single line of data (640 pixels) every 1/15 second. A gray-scale image was then formed by assembling the lines of data into a matrix. The location of the darkest pixel in each line of data corresponded to the location of the water surface. A time series of the surface displacement for the wave with $G = 0.75$ is shown plotted in figure 2.

2.3 Video Recordings and Image Analysis

A Cohu 4915 RS-170 CCD video camera equipped with a Computar 1:1.2 / 12.5 75 mm TV zoom lens was mounted on a tripod so that it viewed the breaking waves from the side through the glass sidewall. The camera was mounted so that it looked up at the underside of the free surface at an angle of approximately 5 degrees. This helped to prevent the rippled and folded surface of the breaking wave crest from obscuring bubbles. A FOR.A VT-22 Video Timer imprinted a time base accurate to 1/100 second directly into the corner of every recorded image. The video signals were recorded in VHS format using a JVC BR-5378U VCR. The breaking waves were backlit by placing a 150 watt spotlight approximately 50 cm behind the far channel wall. A sheet of drafting Mylar was taped to the backside of the far channel wall to diffuse the light. The spotlight was positioned so that the brightest spot of light coincided with the vertical location of the crest as the breaking wave moved through the field of view. This arrangement provided enough light that the aperture of the camera lens could be almost completely closed at the shutter speed of 1/2000 second thus maximizing the depth of field. It also provided more light near the free surface where bubbles were harder to distinguish against the dark background of the free surface.

Fourteen digital images are shown plotted in figure 3 for the freshwater wave with $G = 0.76$. The images in the first column were recorded at camera position 8, the furthest location upstream. The images in the second column were recorded at camera position 1, the furthest location downstream. The images in each column are consecutive and are

separated by 1/30 of a second. The first and second image in each column show the actively breaking crest advancing from right to left. Bubbles are being entrained near the leading edge and are left behind by the fast moving crest. Subsequent images show the evolution of the free surface and the movement of the entrained bubbles. At the upstream location the breaking appears more intense and the free surface is highly distorted. Farther downstream at the breaking at the leading edge is less energetic. It is interesting to note that in images 5 and 6 there are more bubbles at position 1 than at position 8. This is due to the fact that at position 1 bubbles that were entrained upstream are advected into the field of view. At position 8 the wave has just begun to break and therefore no bubbles were advected into the field of view from upstream.

A 2×2 cm grid, as seen in figure 3, was drawn on the glass wall of the channel as an aid in positioning the camera and as a length scale for sizing the bubbles. The camera was positioned so that the lens was 118 cm from the near edge of the channel. The zoom lens was adjusted so that the field of view was 9.4 cm by 6.7 cm. The width of the field of view was smaller than the length of the breaking region and therefore the camera and light were moved along the channel to image the entire wave. Six to eight camera locations were required to cover a given wave. At each location typically nine or ten repeats of the same amplitude wave were recorded. With this set-up it was not possible to determine the position of a bubble across the channel. When computing the bubble size it was assumed that all the bubbles were located at the middle of the channel. Therefore, the computed size of bubbles at the near and far walls are over- and underestimated by 6% respectively. The smallest radius bubbles that could be resolved with this set-up was estimated to be 0.2 mm.

The depth of field was difficult to determine exactly because the aperture of the camera was opened such that without a wave in the field of view the picture was over-exposed. When a breaking wave was present the bubbles and free surface scattered and reflected enough light that the image was not over-exposed, see figure 3. Based upon visual examination of the images the depth of field for bubbles larger than 0.8 mm radius was estimated to be the entire width of the channel, 30 cm.

Bubble sizes and locations were determined by first digitizing the video images using a DT3851 frame grabber board and Global Lab Image software (Data Translation). The images were then processed interactively on a PC. Images were displayed on the computer screen and bubbles and other features were visually identified. The PC pointing device was used to locate and size specific features. The size and location of bubbles was found by selecting two or four points (for spherical or ellipsoidal bubbles respectively) on the circumference of the bubble and then fitting a circle or ellipse to the selected points. The length scale for an image was determined by selecting three of the intersection points of the grid drawn on the near wall of the channel, see figure 3. The lines where the free surface intersected the front and rear glass walls of the channel were determined by selecting approximately ten points along each line. The location of the free surface was taken to be the average of the two lines. The vertical location of the bubbles was computed as the distance below this average free surface location. Using this procedure the vertical location of some bubbles is negative (i.e. above the free surface) and for these cases the bubbles were assumed to be at the free surface.

Bubble size distributions were computed by summing the number of bubbles in 0.2 mm radius increments centred at $r = 0.1, 0.3, 0.5 \dots 4.9$ mm. The volume occupied by the bubbles in each image was computed by dividing the image into ten vertical strips and locating the highest and lowest elevation bubbles in each strip. The volume occupied in each strip equals the height (the elevation difference between the highest and lowest bubbles) times the width of the strip (1/10 of the image width) times the depth of field (channel width, 30 cm). The total volume in each image is the sum of the ten strip volumes. Then for each image the number of bubbles per μm radius bin per m^3 is computed.

3. Results

The water temperature was measured with a Newport model 267B digital thermometers calibrated to ± 0.1 °C. During the course of the experiments the water temperature varied by a maximum of 2 °C for a given wave amplitude and for all wave amplitudes was within the range 20.1 °C to 22.8 °C. These temperature variations are considered negligible because variations this small do not have a significant effect on the process of air entrainment [Hwang *et al*, 1991].

The fractional energy dissipated by breaking is given by,

$$D = (\eta_o^2 - \eta_r^2) / \eta_o^2 \quad (1)$$

where η_o^2 and η_r^2 are the surface displacement variances upstream and downstream of the breaking event [Rapp and Melville, 1990]. Figure 4 shows a plot of the dissipation D as a function of the gain G for both the fresh- and saltwater breaking events. Below the threshold of $G = 0.72$ no breaking occurs and D equals approximately 11.5%, consistent with theoretically predicted losses due to viscous dissipation. The data is very similar to previous measurements of dissipation for dispersive wave packets [Rapp and Melville, 1990; Loewen and Melville, 1991]. The dissipation increases rapidly in the range $G = 0.73$ -0.82, reaching a plateau at $D = 25\%$ and then remains approximately constant for $G > 0.82$. The data in figure 4 show that for a breaking wave of a given amplitude there was no significant difference in the amount of energy dissipated in salt- and freshwater.

Video images of waves with gains of, $G = 0.75, 0.76$ and 0.77 , were analyzed. These amplitudes produce spilling and small plunging breaking waves and correspond to fractional dissipation values of 4% to 6% due to breaking (i.e. after the 11.5% due to viscous dissipation is subtracted). Larger amplitude waves produced bubble clouds that were too dense to analyze accurately with this imaging technique. Ten repeats of each amplitude wave were repeated at each horizontal location of the camera. The third or fourth frame after the breaking wave crest first appeared in the field of view was digitized. In figure 3 image 2 was analyzed because it is the fourth frame after the crest first appeared in the field of view. The images from every other horizontal position were analyzed. A total of 30 to 50 images were analyzed for each wave.

A plot of a typical bubble size distribution (N the number of bubbles per μm radius increment per m^3 versus the bubble radius r) of a freshwater wave with $G = 0.76$ is shown in figure 5. The data are averaged over ten images or repeats of the wave at horizontal position 6 (position 8 is the farthest upstream and position 1 the farthest downstream). The variance in the data is indicated by the error bars which are plus and minus one standard deviation. In figure 6 the bubble size distributions at five horizontal positions for the freshwater wave with $G = 0.77$ are shown plotted. The distributions are similar in shape at the various horizontal positions and the densest distributions occur at positions 4 and 6.

The average bubble size distributions for all six waves are shown plotted in figure 7. The freshwater data in figure 7b clearly show that for a given radius the number of bubbles per unit volume is independent of the amplitude or steepness of the wave packet. The steeper freshwater waves entrain more bubbles but the volume over which they are dispersed also increases and therefore the density of bubbles remains approximately constant. This is not the case for the saltwater data in figure 7a where the size distributions for the largest amplitude packet $G = 0.77$ has consistently higher bubble densities than the two lower amplitude packets for $r > 0.8$ mm.

For all six waves the bubble density increases as the bubble radius r decreases until a maximum value is reached and it then decreases as r decreases further. The location of the maximum bubble density varies from $r = 0.3$ mm - 0.9 mm. Previous investigations have shown that the maximum bubble density typically occurs at a much

smaller radius than indicated in figure 7 [Johnson and Cooke, 1979; Baldy, 1988; Su et al, 1988]. The smallest bubble size which could be detected based on the resolution of the video recordings was $r = 0.2$ mm. However, the data in figure 7 indicate that the imaging technique used here is only consistent down to a bubble radius of $r = 0.8$ mm because some of the bubble size spectra have a maximum at radii as large as 0.9 mm (note that the bin centred at $r = 0.9$ mm covers the range $r = 0.8$ -1.0 mm). In these experiments it was not possible to detect and accurately size all of the bubbles entrained because; (i) smaller bubbles may be hidden behind larger ones, (ii) bubbles very close to the free surface were difficult to detect because of the lack of contrast between the background (the underside of the free surface) and the bubbles, see figure 3, and (iii) the depth of field for bubbles less than $r = 0.8$ mm may have been less than the full width of the channel and therefore small bubbles near the rear channel wall may not have been detected.

The salt- and freshwater data are directly compared in figures 8a-c. The differences between the salt- and freshwater size distributions are small particularly for the two smaller amplitude packets. The largest saltwater wave does have consistently larger bubble densities but given the variance in the data (see figure 5) these differences are not considered significant.

Wave S - salt F - fresh	Gain	Exponential Fit			Power Law Fit		
		β	A_1	Corr. Coeff.	α	A_2	Corr. Coeff.
S	0.77	-1.46	468	0.978	-3.61	222	0.960
S	0.76	-1.54	378	0.972	-3.76	160	0.956
S	0.75	-1.54	341	0.978	-3.68	137	0.962
F	0.77	-1.46	363	0.969	-3.63	167	0.958
F	0.76	-1.42	376	0.964	-3.47	173	0.952
F	0.75	-1.73	489	0.970	-3.79	150	0.945

Table 1. List of constants in the exponential and power law equations fitted to the bubble size distributions, see equations 2 and 3. A least squares procedure was used to fit the equations to the data.

In figure 9 the bubble size distribution for freshwater wave with $G = 0.76$ is plotted. Figure 9a is a semilog plot of N versus r and an exponential equation of the form,

$$N = A_1 e^{\beta r} \quad (2)$$

where A_1 and β are constant has been fitted to the data. Figure 9b is a log-log plot of N versus r and a power law equation of the form,

$$N = A_2 r^\alpha \quad (3)$$

where A_2 and α are constants has been fitted to the data. In table 1 the constants A_1 , β , A_2 and α and the correlation coefficients for the exponential and power law equations are listed for the six waves. The average value of the exponents are $\beta = -1.5$ and $\alpha = -3.7$. The correlation coefficients for the power law fits are in the range from 0.94 to 0.96 and for the exponential fits they are consistently higher in the range from 0.96 to 0.98. Note that only the data for $r \geq 0.8$ mm was included in the correlations (i.e. the first four data points corresponding to bins at $r = 0.1, 0.3, 0.5$ and 0.7 mm were excluded). The data in table 1 indicate that either equation 2 or 3 provides a good fit to the observed data.

If the bubble size distribution data plotted in figure 7 is multiplied by $4/3\pi r^3$ then N , the number of bubbles per μm radius per m^3 of volume, is transformed to V , the bubble volume divided by the total volume in per μm radius. The void fraction is defined

as the bubble volume divided by the total volume therefore V can be interpreted as the void fraction per μm radius increment or the contribution to the total void fraction from bubbles of a particular size. Plots of V versus r for the fresh- and saltwater breakers are presented in figure 10. The area under the curves is the average void fraction for each wave. The average void fraction for the six waves is tabulated in table 2. All of the curves for both the fresh- and saltwater waves have a maximum at a radius of approximately 2 mm. These plots indicate that bubbles in the size range $r = 1\text{-}3$ mm contribute the most to the entrained volume or void fraction in both salt- and freshwater.

The energy required to submerge a single bubble of radius r to a depth of z is given by,

$$e_b = \frac{4}{3} \pi r^3 \gamma z \quad (4)$$

where γ is the specific weight of water and e_b is the energy in Joules. The amount of wave energy dissipated by a breaking wave can be approximated by,

$$E_w = \frac{1}{2} \gamma C_g b T_w \eta_d^2 \quad (5)$$

where T_w is the length of the sampling interval, η_d^2 is the difference between the upstream and downstream surface displacement variance, C_g is the group velocity of the center component of the wave packet and b is the width of the wave channel [Loewen and Melville, 1991]. E_b is defined as the energy required to submerge all the bubbles entrained by an individual breaking wave. The values of E_b and E_w were computed for the six waves and are tabulated in table 2 along with the ratio E_b/E_w .

Wave		Average Void Fraction	E_w (J)	E_b (J)	E_b/E_w
S - salt F - fresh	Gain				
S	0.77	2.6×10^{-3}	0.52	2.2×10^{-3}	4.2×10^{-3}
S	0.76	1.7×10^{-3}	0.52	1.2×10^{-3}	2.3×10^{-3}
S	0.75	1.5×10^{-3}	0.48	7.4×10^{-4}	1.5×10^{-3}
F	0.77	2.0×10^{-3}	0.59	1.9×10^{-3}	3.2×10^{-3}
F	0.76	2.2×10^{-3}	0.56	1.1×10^{-3}	2.0×10^{-3}
F	0.75	1.3×10^{-3}	0.51	2.5×10^{-4}	4.9×10^{-4}

Table 2: The average void fraction for the six breaking waves, E_w is the energy dissipated by breaking and E_b is the energy required to submerge the bubbles..

The distribution of the total number of bubbles (i.e. of all sizes) as a function of depth below the free surface is shown plotted in figure 11. There are no significant differences between the depth distribution in saltwater and freshwater. The two depth distributions can be fitted with an equation of the form,

$$N(z) = N_0 e^{-z/h} \quad (6)$$

where N_0 is the total bubble density at the free surface and h is the entrainment depth

[Hwang *et al.*, 1990]. For the saltwater depth distribution $N_0 = 3.9 \times 10^5$ per m^3 and $h = 1.0$ cm and for the freshwater depth distribution $N_0 = 4.7 \times 10^5$ per m^3 and $h = 0.94$ cm.

4. Discussion

The fact that the measured bubble size distributions were so similar in fresh- and saltwater is a surprising result. Many previous studies have observed significant differences between the bubble size distributions in fresh- and saltwater. *Cartmill and Su* [1993] observed that beneath large (wave height = 1.2 m) mechanically generated plunging breaking waves the shape of the bubble size distributions were the same in fresh- and saltwater. However, they found that there were approximately a factor of ten more bubbles per unit volume in the saltwater than in the freshwater. *Haines and Johnson* [1995] also observed large differences in the size distribution in salt- and freshwater. They simulated a breaking wave using an intermittent waterfall produced by a tipping bucket suspended 70 cm above the surface of the main tank. In seawater 99% of the bubbles were observed to have radii smaller than 1.5 mm and in freshwater only 67% of the bubbles had radii smaller than 1.5 mm. They found that the number of bubbles per unit volume in seawater was approximately four times greater than in freshwater.

One possible explanation for this apparent discrepancy is that the breaking events produced in our experiments were very gentle spilling breakers compared to the more energetic breakers produced in the other two experiments. The maximum depth to which bubbles were entrained in our experiments was 6 cm. In *Cartmill and Su's* [1993] experiment the breaking events were large energetic plunging waves which entrained bubbles to depths greater than 73 cm. *Haines and Johnson* [1995] observed bubbles to depths up to 30 cm beneath the intermittent waterfall. The turbulent flow field produced by gently spilling waves would be much less intense than that produced by large plunging breakers or by tipping a 800 ml bucket of water from a height of 70 cm. The observed differences between the bubble size distributions in salt- and freshwater has been attributed to the coalescence of small bubbles in freshwater [Scott, 1975]. Therefore, it may be that in the absence of an energetic turbulent flow field there is no mechanism for the production of smaller bubbles and hence no opportunity for the smaller bubbles to coalesce in freshwater. That is, the same bubble sizes are produced at the surface in salt- and freshwater and it is the subsequent action of the flow field on the bubbles which leads to the observed differences in the bubble size distributions.

In addition, in our experiments images of the region immediately behind the breaking crest were analyzed to determine the bubble size distributions. The average distributions for a given wave were obtained by ensemble averaging over many repeats of the same breaking event. This is in contrast to the experiments of *Cartmill and Su* [1993] in which the bubble size distributions are obtained by time averaging over periods comparable to or longer than the wave period. The fact that the bubble size distributions obtained by time averaging and ensemble averaging do not agree is not particularly surprising. It simply means that the process of air entrainment is not ergodic.

Hwang et al [1990] and *Baldy and Bourguel* [1987] investigated air entrainment by breaking wind waves in laboratory wave tanks. In both studies the slope of the bubble size distributions were observed to vary from -2, near the free surface to -4, deeper in the water column. In this study we found that the slope of the bubble size distributions were approximately -3.7 for bubble radii > 0.8 mm. The difference in the slopes may be due to the fact that the maximum radius of bubbles observed in the other two studies was 1.5 mm considerably less than the maximum of 5 mm observed in our experiments. *Hwang et al* [1990] and *Baldy and Bourguel* [1987] present time-averaged bubble size distributions computed by averaging over long time periods compared to the period of the waves therefore direct comparisons to the ensemble-averaged results presented here may not be valid.

The depth to which bubbles are entrained is characterized by the entrainment depth or e-folding depth of the bubble depth distribution as defined in equation 6. *Hwang et al* [1990] found that h varied from 5.4 - 10.8 cm for wind waves with rms wave amplitudes from 1.7 - 2.7 cm. *Baldy and Bourguel* [1987] did not compute the entrainment depth but it can be computed from the data in their figure 12 for wind waves with a significant wave height of 9.2 cm at a wind speed of 14 m/s. The entrainment depth for this case is $h = 1.1$ cm. In our experiments we found $h = 1.0$ cm and 0.94 cm for the salt- and freshwater waves respectively in agreement with the measurements of *Baldy and Bourguel* [1987]. It is not surprising that the entrainment depths observed by *Hwang et al* [1990] do not agree with the other measurements because their measurements were all taken below the minimum trough level of the waves.

In table 2, E_w , the amount of wave energy dissipated and, E_b , the amount of energy required to submerge the observed bubbles and the ratio of E_b/E_w are shown tabulated. The fraction of wave energy that is dissipated by breaking that goes into submerging the bubbles is very small for these gently spilling waves. It varies from 0.05% to 0.4% which is much smaller than the values 30% to 50% observed by *Lamarre and Melville* [1991]. In their experiments the waves were much steeper plunging breakers and the bubbles were entrained to depths of 40-50 cm. Our results indicate that if the breaking events are of the spilling type then a much smaller fraction of the dissipated energy is expended in submerging bubbles.

5. Conclusions

We have reported on the measurements of the large bubble size distributions in fresh- and saltwater beneath mechanically generated breaking wave packets. It was found that the size distribution for large bubbles, $r > 0.8$ mm, are essentially the same in salt- and freshwater. The bubble spectra are best represented by an exponential equation of the form $N \sim e^{-1.5r}$ or alternatively by a power law equation of the form $N \sim r^{-3.7}$. The depth distributions in salt- and freshwater are very similar and may be represented by an exponential equation, $N = 4 \times 10^5 e^{-z}$. These measurements demonstrate that significant numbers of large bubbles are entrained beneath small-scale breaking waves (wavelengths of ~ 1.5 m and amplitudes of ~ 10 cm). These results combined with *Keeling's* [1993] predictions suggest that air-sea gas transfer due to the entrainment of large bubbles may be significant even when the sea surface is relatively calm.

Acknowledgments

We would like to thank D. Doede for assisting in the experiments and the data processing. This research was funded by a grant from the Natural Sciences and Engineering Research Council of Canada.

References

- Baldy, S., Bubbles in the close vicinity of breaking waves, *J. Geophys. Res.* 93, 8239-8248, 1988.
- Baldy, S. and M. Bourguel, Bubbles between the wave trough and wave crest levels, *J. Geophys. Res.*, 92, 2919, 1987.
- Blanchard, D.C. and L.D. Syzdek, Mechanism for the water-to-air transfer and concentration of bacteria, *Science*, 170, p.626-628, 1970.
- Blanchard, D.C. and A.H. Woodcock, Bubble formation and modification in the sea and its meteorological significance, *Tellus*, 9, p.145-158, 1957.
- Chan, E.S. and W.K. Melville, Deep-water plunging wave pressures on a vertical plane wall, *Proc. R. Soc. Lond.*, A417, p. 95-131, 1988.

Loewen, O'Dor and Skafel, submitted to JGR, November, 1995.

- Cipriano, R. and D.C. Blanchard, Bubble and aerosol spectra produced by a laboratory breaking wave, *J. Geophys. Res.*, 86, 8085-8092, 1981.
- Farmer, D.M., C.L. McNeil and B.D. Johnson, Evidence for the importance of bubbles to the enhancement of air-sea gas flux, *Nature*, v.361, p.620-623, 1993.
- Haines, M.A. and B.D. Johnson, Injected bubble populations in seawater and freshwater measured by a photographic method, *J. Geophys. Res.*, 100, 7057-7068, 1995.
- Hwang, P.A., Y.-H. L. Hsu and J. Wu, Air bubbles produced by breaking wind waves: A laboratory study, *J. Phys. Oceanogr.*, 20, 19-28, 1990.
- Hwang, P.A., Y.-K. Poon and J. Wu, Temperature effects on generation and entrainment of bubbles induced by a water jet, *J. Phys. Oceanogr.*, 21, 1602-1605, 1991.
- Johnson, B.D. and R.C. Cooke, Bubble populations and spectra in coastal waters: A photographic approach, *J. Geophys. Res.*, 84, 3761-3766, 1979.
- Keeling, R.F., On the role of large bubbles in air-sea gas exchange and supersaturation in the ocean, *J. Marine Res.*, 51, p.237-271, 1993
- Kerman, B.R., Sea Surface Sound - Natural Mechanisms of Surface Generated Noise in the Ocean, Kluwer, Dordrecht, 1988.
- Kolovayev, P.A., Investigation of the concentration and statistical size distribution of wind-produced bubbles in the near-surface ocean layer, *Oceanology*, 15, p.659-661, 1976.
- Lamarre, E. and W.K. Melville, Air entrainment and dissipation in breaking waves, *Nature*, 351, p. 469-472 (1991).
- Lamarre, E. and W.K. Melville, Void-fraction measurements and sound-speed fields in bubble plumes generated by breaking waves, *J. Acoust. Soc. Am.*, 95 (3), 1317-1328, 1994.
- Loewen, M.R., M.A. O'Dor and M.G. Skafel, "Laboratory measurements of bubble size distributions under breaking waves", *Third International Symposium on Air-Water Gas Transfer*, University of Heidelberg, July 24-27, 1995 (in press).
- Loewen, M.R. and W.K. Melville, An experimental investigation of the collective oscillations of bubble plumes entrained by breaking waves, *J. of the Acoust. Soc. of Am.*, 95 (3), p.1329-1343, 1994.
- Loewen, M.R. and W.K. Melville, Microwave backscatter and acoustic radiation from breaking waves, *J. Fluid Mech.*, 224, 601-623, 1991.
- Medwin, H. and N.D. Breitz, Ambient and transient bubble spectral densities in quiescent seas and under spilling breakers, *J. Geophys. Res.*, 94, p.12,751-12,759, 1989.
- Monahan, E.C. and C.R. Zietlow, Laboratory comparisons of freshwater and saltwater whitecaps, *J. Geophys. Res.*, 74, 6961-6966, 1969.
- Rapp, R.J. and W.K. Melville, Laboratory measurements of deep water breaking waves, *Phil. Trans. Royal Society of London*, A331, p. 735-800, 1990.
- Scott, J.C., The role of salt in whitecap persistence, *Deep Sea Res.*, 22, p.653-657, 1975.
- Su, M.Y., S.C. Ling, and J. Cartmill, Optical microbubble measurements in the north sea, *Sea Surface Sound - Natural Mechanisms of Surface Generated Noise in the Ocean*, ed. B.R. Kerman, Kluwer, Dordrecht, p.211-224, 1988.
- Thorpe, S.A., The role of bubbles produced by breaking waves in super-saturating the near-surface ocean mixing layer with oxygen, *Ann. Geophys.*, 2, 53-56, 1984.
- Wallace, D.W.R. and C.D. Wirick, Large air-sea gas fluxes associated with breaking waves, *Nature*, v.356, p.694-696, 1992.

Figure 1. Schematic of the wave channel and experimental equipment.

Figure 2: Plot of 400 lines of video data showing the times series of the salt water wave with gain $G = 0.75$ at a distance of $x = 5$ m from the wave paddle. The vertical lines of data are separated by 1/15 second.

Figure 3: Digital video images of the saltwater breaking wave of gain $G = 0.76$. The images in each column are separated by 1/30 second. Column I has a series of images recorded at position 8 (furthest upstream) and column II a series recorded at position 2 (furthest downstream). The waves are moving from left to right and the leading edge of the active breaking crest is visible in the first two images in each series. The grid drawn on the glass channel wall is 2 cm x 2 cm.

Figure 4: The fractional energy dissipated D in percent plotted versus the wave gain G . The error bars are plotted for plus and minus one standard deviation for the freshwater waves. o - freshwater, x - saltwater.

Figure 5: The bubble size spectrum, N the number of bubbles per μm radius increment per m^3 versus r the bubble radius, for the saltwater wave with $G = 0.76$ at position 6. The data were obtained by averaging over ten repeats i.e. ten images. The radius bins are 0.2 mm wide centred at 0.1, 0.3 4.9 mm. The error bars denote plus or minus one standard deviation.

Figure 6: The bubble size spectrum, N the number of bubbles per μm radius increment per m^3 versus r the bubble radius, for the freshwater wave with $G = 0.77$ at horizontal positions 1, 2, 4, 6 and 8. The data were obtained by averaging over ten repeats i.e. ten images. The radius bins are 0.2 mm wide centred at 0.1, 0.3 4.9 mm. Position 1 is upstream and 8 is downstream. Position 1 - o, 2 - x, 4 - *, 6 - +, 8 - \oplus .

Figure 7: The average bubble size distribution, N the number of bubbles per μm radius increment per m^3 versus r the bubble radius in mm, for (a) the three saltwater waves and, (b) the three freshwater waves. The radius bins are 0.2 mm wide centred at 0.1, 0.3 4.9 mm. + - $G = 0.77$, x - $G = 0.76$ and o - $G = 0.75$

Figure 8: A comparison of the bubble size distributions, N (number per μm per m^3) versus r (mm), in salt- and freshwater. Plots (a), (b) and (c) correspond to gains of 0.75, 0.76 and 0.77 respectively. + - freshwater, o - saltwater.

Figure 9: Bubble size distribution for a freshwater wave with $G = 0.76$. (a) An exponential equation has been fitted to the data and (b) a power law equation has been fitted to the data. Note that points corresponding to the smallest four radius bins (0.1 - 0.7 mm) have not been used to compute the least square fits.

Figure 10: V , the bubble volume / total volume (void fraction) per μm radius increment per m^3 versus the bubble radius r in mm. (a) Freshwater and (b) saltwater breaking waves. o - $G = 0.75$, x - $G = 0.76$, + - $G = 0.77$

Figure 11: N_p , the total number of bubbles per m^3 ($r > 0.8$ mm) plotted versus the depth d in cm below the free surface. o - saltwater, x - freshwater.

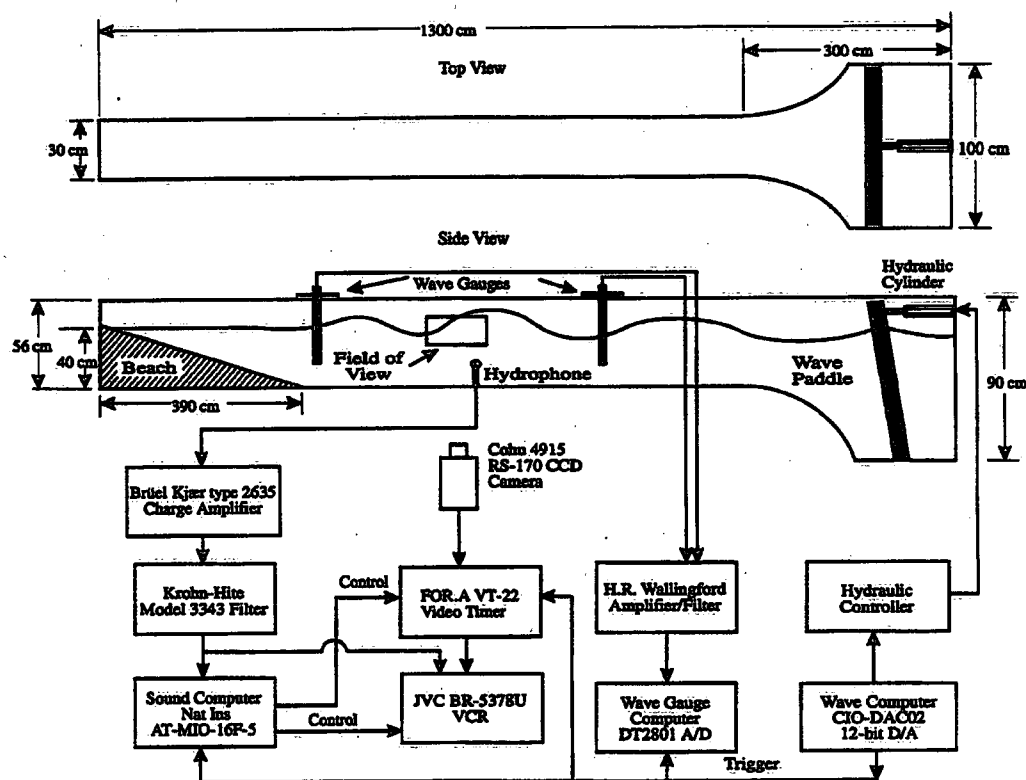


Figure 1. Schematic of the wave channel and experimental equipment.

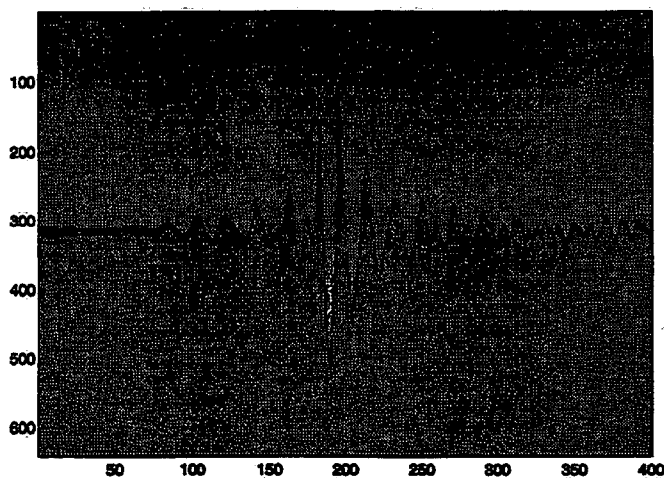
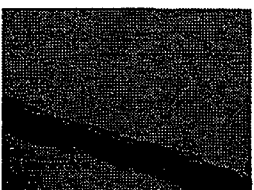


Figure 2: Plot of 400 lines of video data showing the times series of the salt water wave with gain $G = 0.75$ at a distance of $x = 5$ m from the wave paddle. The vertical lines of data are separated by $1/15$ second.

Figure 3: Digital video images of the saltwater breaking wave of gain $G = 0.76$. The images in each column are separated by 1/30 second. Column I has a series of images recorded at position 8 (furthest upstream) and column II a series recorded at position 2 (furthest downstream). The waves are moving from left to right and the leading edge of the active breaking crest is visible in the first two images in each series. The grid drawn on the glass channel wall is 2 cm x 2 cm.

I



II



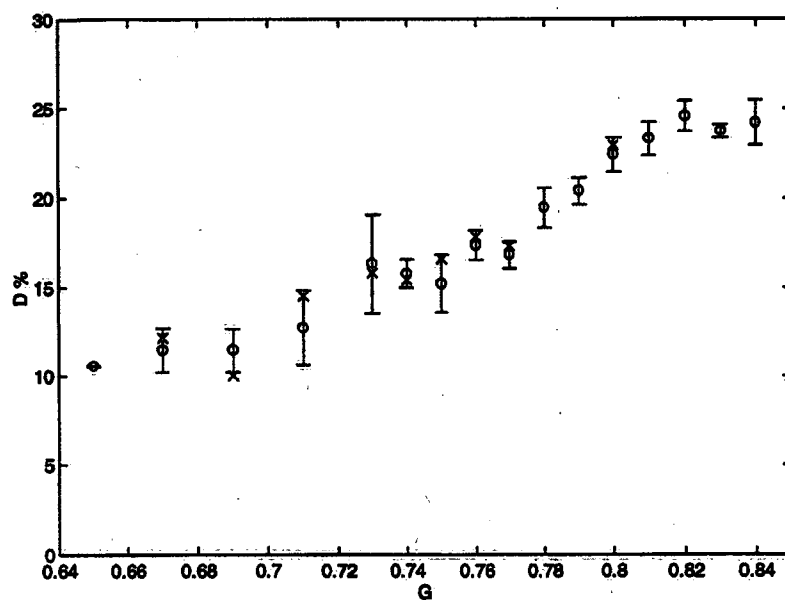


Figure 4: The fractional energy dissipated D in percent plotted versus the wave gain G . The error bars are plotted for plus and minus one standard deviation for the freshwater waves. o - freshwater, x - saltwater.

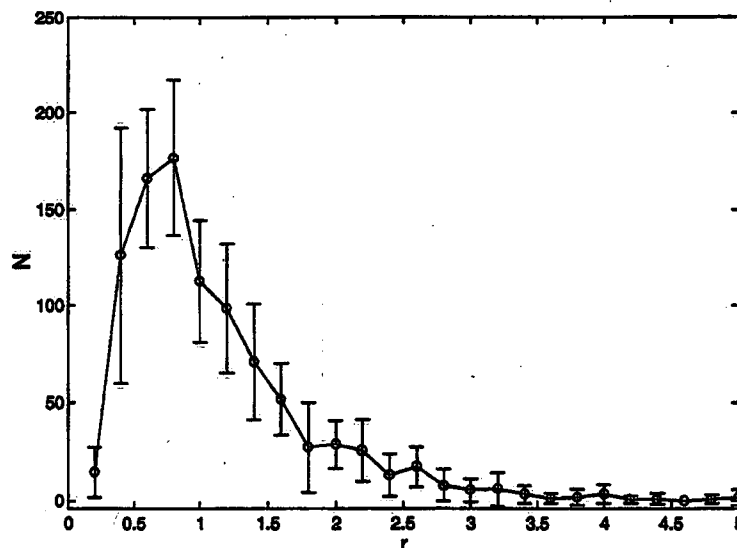


Figure 5: The bubble size spectrum, N the number of bubbles per μm radius increment per m^3 versus r the bubble radius, for the saltwater wave with $G = 0.76$ at position 6. The data were obtained by averaging over ten repeats i.e. ten images. The radius bins are 0.2 mm wide centred at 0.1, 0.3 4.9 mm. The error bars denote plus or minus one standard deviation.

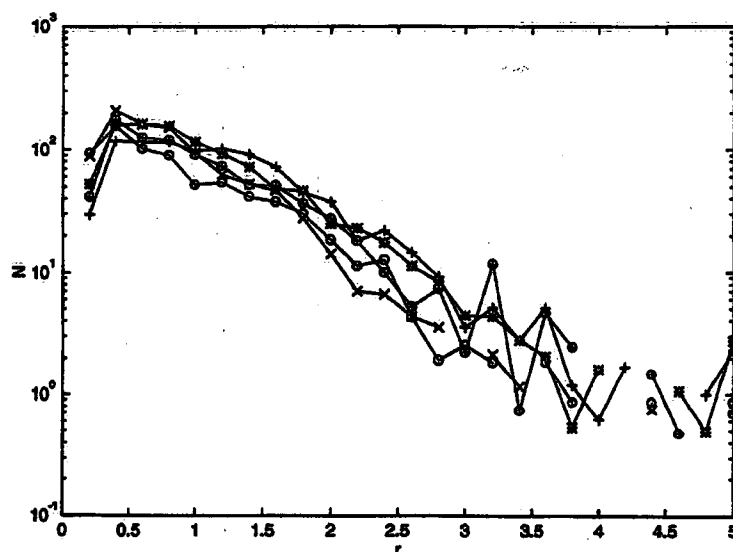


Figure 6: The bubble size spectrum, N the number of bubbles per μm radius increment per m^3 versus r the bubble radius, for the freshwater wave with $G = 0.77$ at horizontal positions 1, 2, 4, 6 and 8. The data were obtained by averaging over ten repeats i.e. ten images. The radius bins are 0.2 mm wide centred at 0.1, 0.3 4.9 mm. Position 1 is upstream and 8 is downstream. Position 1 - o, 2 - x, 4 - *, 6 - +, 8 - \oplus .

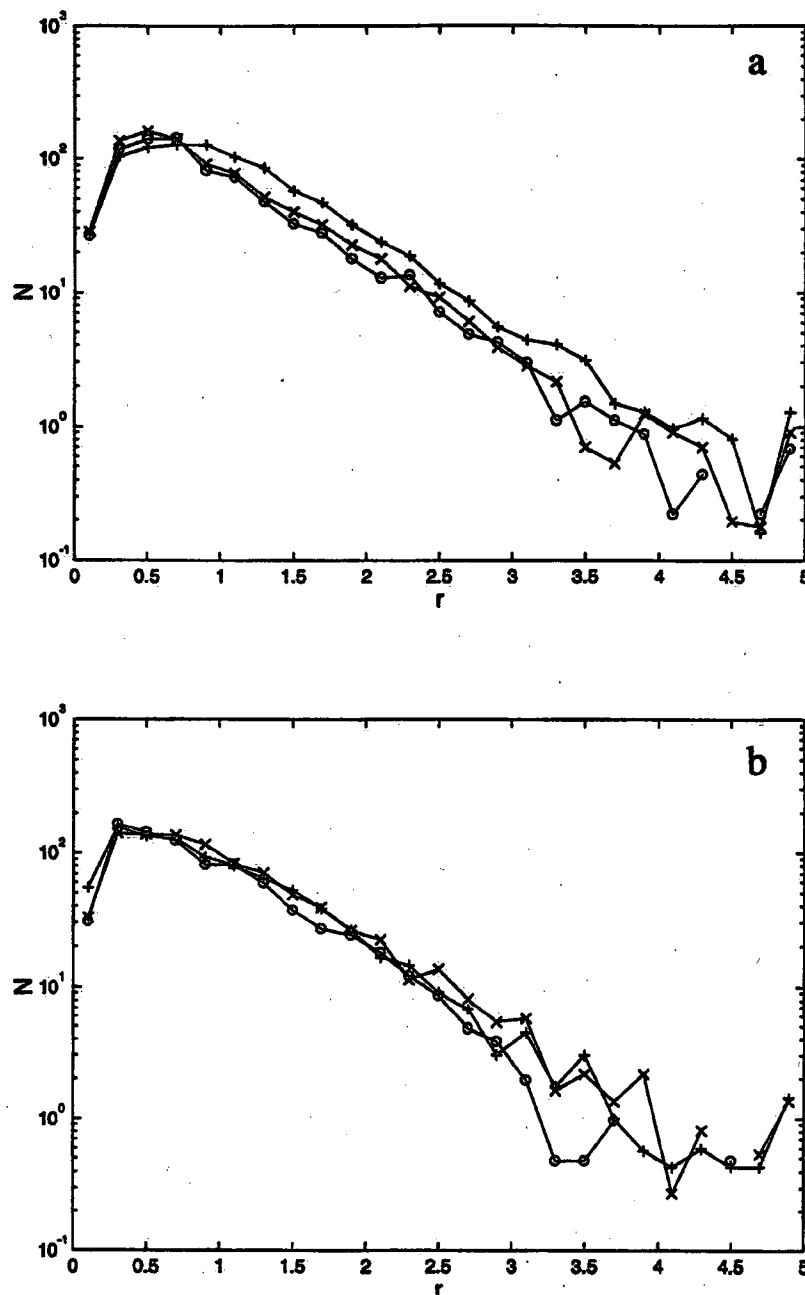


Figure 7: The average bubble size distribution, N the number of bubbles per μm radius increment per m^3 versus r the bubble radius in mm, for (a) the three saltwater waves and, (b) the three freshwater waves. The radius bins are 0.2 mm wide centred at 0.1, 0.3 4.9 mm. + - $G = 0.77$, x - $G = 0.76$ and o - $G = 0.75$

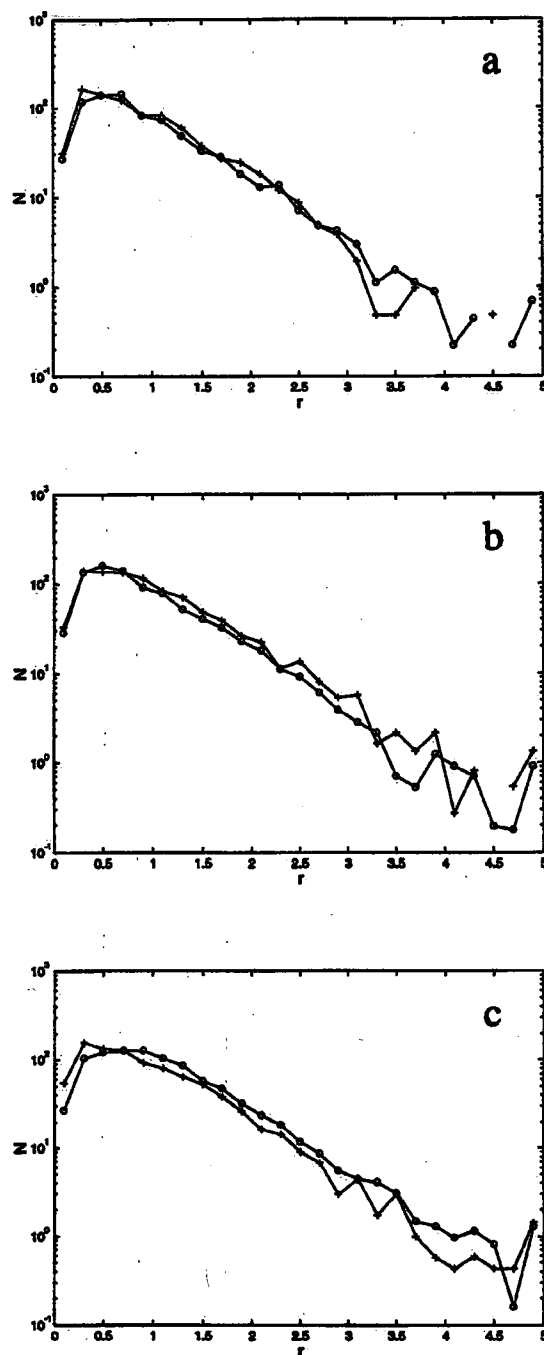


Figure 8: A comparison of the bubble size distributions, N (number per μm per m^3) versus r (mm), in salt- and freshwater. Plots (a), (b) and (c) correspond to gains of 0.75, 0.76 and 0.77 respectively. + - freshwater, o - saltwater.

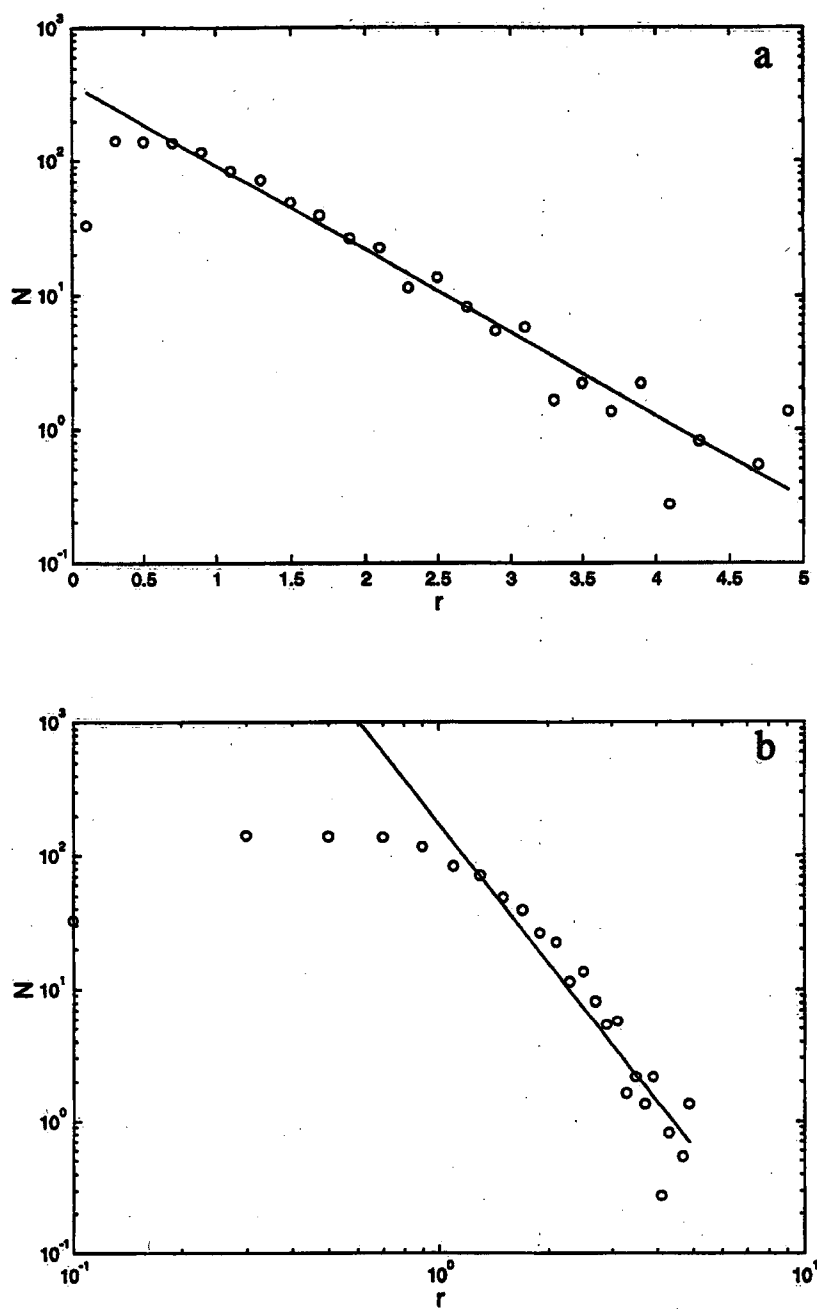


Figure 9: Bubble size distribution for a freshwater wave with $G = 0.76$. (a) An exponential equation has been fitted to the data and (b) a power law equation has been fitted to the data. Note that points corresponding to the smallest four radius bins (0.1 - 0.7 mm) have not been used to compute the least square fits.

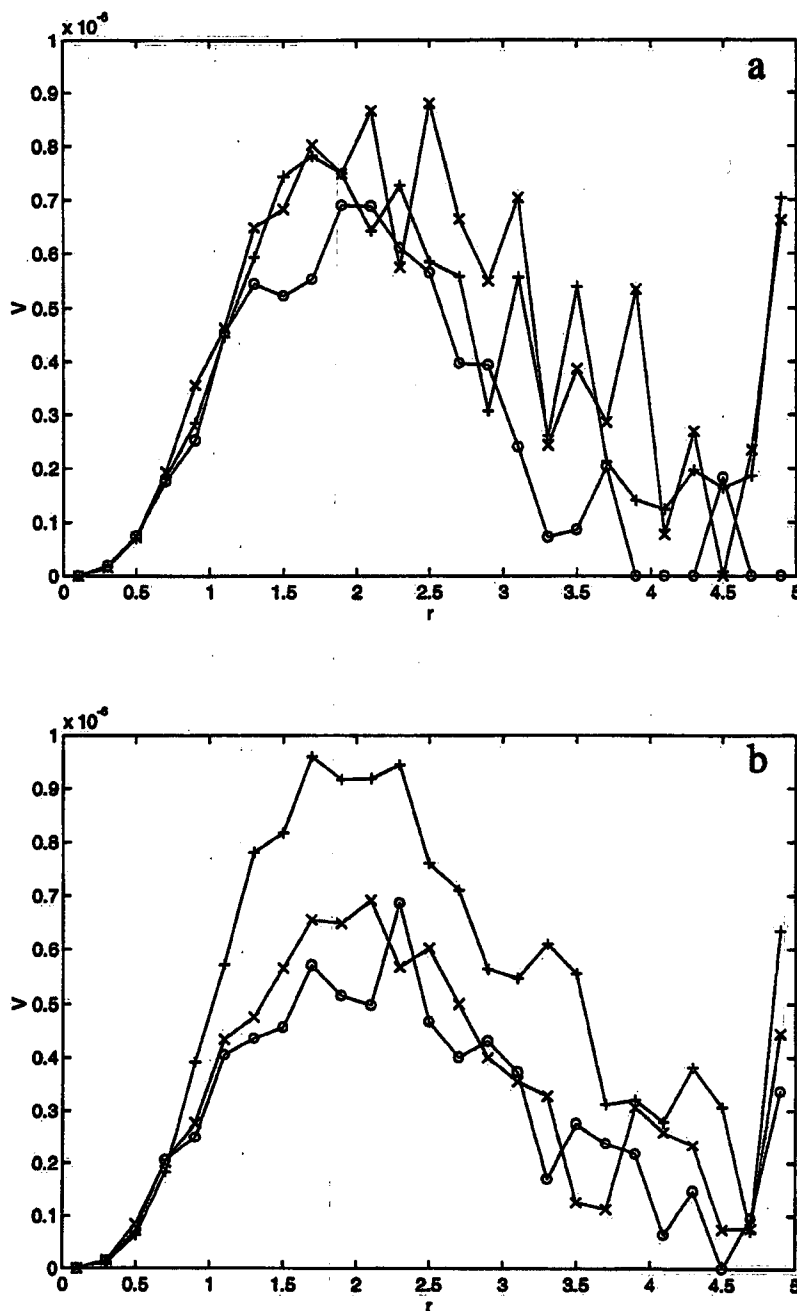


Figure 10: V , the bubble volume / total volume (void fraction) per μm radius increment per m^3 versus the bubble radius r in mm. (a) Freshwater and (b) saltwater breaking waves. o - $G = 0.75$, x - $G = 0.76$, + - $G = 0.77$

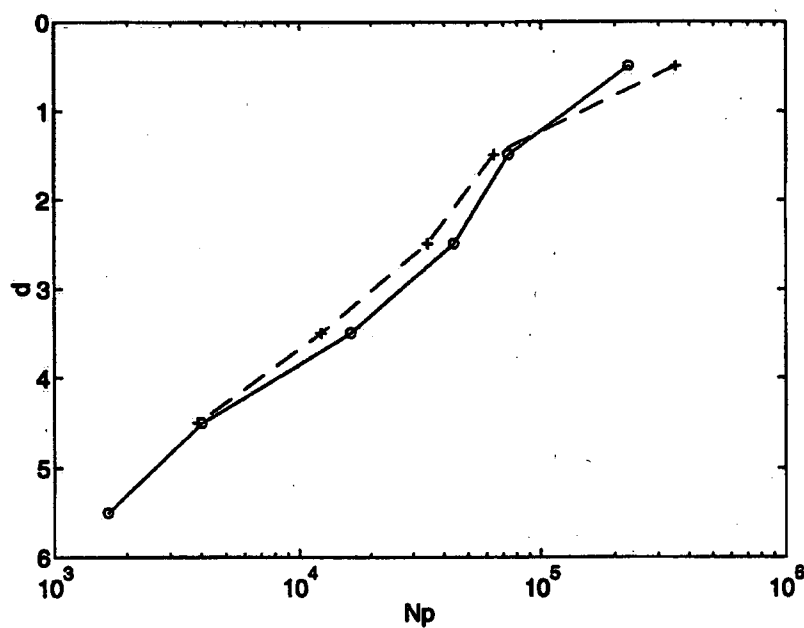


Figure 11: N_p the total number of bubbles per m^3 ($r > 0.8 \text{ mm}$) plotted versus the depth d in cm below the free surface. o - saltwater, x - freshwater.

Environment Canada Library, Burlington



3 9055 1017 8206 7



Environment
Canada

Environnement
Canada

Canada

Canada Centre for Inland Waters

P.O. Box 5050
867 Lakeshore Road
Burlington, Ontario
L7R 4A6 Canada

National Hydrology Research Centre

11 Innovation Boulevard
Saskatoon, Saskatchewan
S7N 3H5 Canada

St. Lawrence Centre

105 McGill Street
Montreal, Quebec
H2Y 2E7 Canada

Place Vincent Massey

351 St. Joseph Boulevard
Gatineau, Quebec
K1A 0H3 Canada

Centre canadien des eaux intérieures

Case postale 5050
867, chemin Lakeshore
Burlington (Ontario)
L7R 4A6 Canada

Centre national de recherche en hydrologie

11, boul. Innovation
Saskatoon (Saskatchewan)
S7N 3H5 Canada

Centre Saint-Laurent

105, rue McGill
Montréal (Québec)
H2Y 2E7 Canada

Place Vincent-Massey

351 boul. St-Joseph
Gatineau (Québec)
K1A 0H3 Canada